Monthly Notices of the ROYAL ASTRONOMICAL SOCIETY

MNRAS **450,** 2132–2142 (2015) doi:10.1093/mnras/stv765

The stellar kinematics of corotating spiral arms in *Gaia* mock observations

Jason A. S. Hunt,[1]★ Daisuke Kawata,[1] Robert J. J. Grand,[2,3] Ivan Minchev,[4] Stefano Pasetto[1] and Mark Cropper[1]

[1]*Mullard Space Science Laboratory, University College London, Holmbury St. Mary, Dorking, Surrey RH5 6NT, UK*
[2]*Heidelberger Institut fur Theoretische Studien, Schloss-Wolfsbrunnenweg 35, D-69118 Heidelberg, Germany*
[3]*Zentrum für Astronomie der Universität Heidelberg, Astronomisches Recheninstitut, Mönchhofstr. 12-14, D-69120 Heidelberg, Germany*
[4]*Leibniz-Institut für Astrophysik Potsdam (AIP), An der Sternwarte 16, D-14482 Potsdam, Germany*

Accepted 2015 April 7. Received 2015 March 31; in original form 2014 December 22

ABSTRACT

We have observed an *N*-body/smoothed particle hydrodynamics simulation of a Milky Way-like barred spiral galaxy. We present a simple method that samples *N*-body model particles into mock *Gaia* stellar observations and takes into account stellar populations, dust extinction and *Gaia*'*s* science performance estimates. We examine the kinematics of stars with $V \leq 16$ mag around a nearby spiral arm at a similar position to the Perseus arm at three lines of sight in the disc plane; $(l, b) = (90, 0)$, (120, 0) and (150, 0) deg. We find that the structure of the peculiar kinematics around the corotating spiral arm, which is found in Kawata et al. (2014b), is still visible in the observational data expected to be produced by *Gaia*, despite the dust extinction and expected observational errors of *Gaia*. These observable kinematic signatures will enable testing whether the Perseus arm of the Milky Way is similar to the corotating spiral arms commonly seen in *N*-body simulations.

Key words: methods: numerical – Galaxy: structure – galaxies: kinematics and dynamics – galaxies: structure.

1 INTRODUCTION

The spiral features visible in many galaxies have long been the subject of debate. Although it has been almost a century since the resolution of the 'great debate' of Shapley & Curtis (1921), when it was argued over whether these beautiful spiral structures were nebulae within our galaxy or galaxies in their own right, the mechanisms which generate them are still uncertain. One of the problems with developing a comprehensive theory of spiral arms is the so-called winding dilemma. It is known from observations of disc galaxies that the stars in the inner region have a higher angular velocity than those in the outer region. Therefore, the spiral structure should 'wind up' relatively quickly if the spiral arms rotate at the mean rotation velocity of the stars (e.g. Wilczynski 1896), contrary to observations of many 'grand design' spiral galaxies. A proposed solution to the winding dilemma is given by spiral density wave theory (Lin & Shu 1964) which treats the spiral structure as a density wave which can rotate rigidly as a feature with a constant pattern speed and thus be long-lived.

However, no *N*-body simulations have yet been able to reproduce these long-lived stable spiral arms, despite the increase in computational power and resolution which has occurred in recent years (e.g. Sellwood 2011; Dobbs & Baba 2014). Recent work has shown spiral modes and waves which survive over multiple rotations (Quillen et al. 2011; Roškar, Debattista & Loebman 2013; Sellwood & Carlberg 2014) while the spiral arm features in the stellar mass are short-lived but recurrent (e.g. Sellwood & Carlberg 1984; Carlberg & Freedman 1985; Bottema 2003; Fujii et al. 2011; Grand, Kawata & Cropper 2012a,b, 2013; Baba, Saitoh & Wada 2013; D'Onghia, Vogelsberger & Hernquist 2013; Roca-Fàbrega et al. 2013) including in galaxies with a central bar (e.g. Grand et al. 2012b), implying that the large spiral arms visible in external galaxies may only *appear* to be rigid structures extending over the disc, while in fact being made of transient reforming features.

The interpretation of the transient and recurrent spiral arm features observed in *N*-body simulations is still in debate. For example, Minchev et al. (2012) showed for the first time (by studying the time evolution of the disc power spectrum) that spiral wave modes in *N*-body simulations can last for as long as 1 Gyr, which can justify treating the wave modes as quasi-stationary structure, and the transient and recurrent spiral arm features can be explained by the superposition of different modes with different pattern speeds (see also Roškar et al. 2012; Sellwood & Carlberg 2014). On the other hand, Grand et al. (2012a), D'Onghia et al. (2013) and Baba et al. (2013) demonstrated non-linear growth of the spiral arm

★ E-mail: jash2@mssl.ucl.ac.uk

features due to similar but different (in terms of evolution) mechanisms from swing amplification (Toomre 1981), which could be difficult to explain with the linear superposition of the wave modes.

Our position within the Milky Way gives us a unique view of these spiral structures seen in external galaxies, but it comes with its own set of problems which we must overcome when studying them. The location and kinematics of the gaseous component of the arms may be determined from HI and CO observations (e.g. Dame, Hartmann & Thaddeus 2001; Nakanishi & Sofue 2003; Kalberla & Kerp 2009). However, to observe the kinematics of the stellar component in and around the spiral arms we must look through the disc plane, which carries the heaviest levels of dust and gas, and thus high levels of extinction.

Dust extinction has long been a problem for Milky Way model construction. Although there are reasonably reliable extinction maps for extragalactic sources whose extinction by the interstellar medium of the Milky Way can be corrected as a function $A_\lambda(l, b)$ (e.g. Schlegel, Finkbeiner & Davis 1998), three-dimensional extinction mapping for sources within the Milky Way i.e. $A_\lambda(l, b, d)$ is more challenging. There are three-dimensional extinction maps for individual sections of the sky (e.g. Drimmel & Spergel 2001; Marshall et al. 2006; Hanson & Bailer-Jones 2014; Sale & Magorrian 2014) and two-dimensional maps have been extended to three dimensions (e.g. Drimmel, Cabrera-Lavers & López-Corredoira 2003). However, a truly Galactic 3D extinction map does not yet exist (Rix & Bovy 2013). The European Space Agency (ESA)'s *Gaia* mission will help us map the stellar structure and kinematics of the Milky Way, and help constrain extinction at the same time (Bailer-Jones et al. 2013).

Gaia, which was launched on 2013 December 19 will provide detailed astrometric (e.g. Lindegren et al. 2012), spectroscopic (e.g. Katz et al. 2011) and photometric (e.g. Jordi et al. 2010) information for around one billion stars in the Milky Way. Detailed information on *Gaia* scientific accuracies is available in, for example, de Bruijne (2012). Synthetic *Gaia* mock data have already been used to demonstrate different applications of the real *Gaia* data set. For example, Abedi et al. (2014) use three tracer populations (OB, A and Red Clump stars) with the *Gaia* selection function, errors and dust extinction, and demonstrated that the *Gaia* mock data can recover the parameters of the Galactic warp. Romero-Gómez et al. (2015) examine the Galactic bar in the *Gaia* observable space using Red Clump tracers with the *Gaia* selection function, errors and dust extinction. In Hunt & Kawata (2014), we show that we can recover the large-scale structure of the Galactic disc with our made-to-measure galaxy modelling code, PRIMAL(Hunt, Kawata & Martel 2013; Hunt & Kawata 2013, 2014), and make a good estimation of the pattern speed of the bar, using tracer populations of M0III and Red Clump stars with the *Gaia* selection function, errors and dust extinction.

There exist full mock catalogues of *Gaia* stars, e.g. the *Gaia* Universe Model Snapshot (GUMS) which provides a view of the Besançon Galaxy model as seen from *Gaia* (Robin et al. 2012), taking into account dust extinction while assuming there are no observational errors. This detailed prediction of *Gaia* observations gives an excellent indication of the volume and quality of data which will become available from *Gaia*, predicting 1.1 billion observable stars, almost 10 000 times more than from its predecessor *Hipparcos*. GUMScan be extended through the *Gaia* Object Generator (GOG; Luri et al. 2014) to simulate intermediate and final catalogue data including the introduction of realistic astrometric, photometric and spectroscopic observational errors to the catalogue based upon *Gaia* science performance estimates. While these mock data provide an excellent example of the capabilities of *Gaia*, the Besançon galaxy model is an axisymmetric model and a kinematic model not a dynamical model. Although *Gaia* will not provide accelerations, the kinematics it will provide are from a dynamical system, the Milky Way. Thus, it is important for our purpose to generate catalogues from fully dynamical models with non-axisymmetric structures, such as spiral arms and a bar, which for example *N*-body disc galaxy models can provide.

Therefore, we propose here to create mock *Gaia* observations from an *N*-body model using a population synthesis code such as GALAXIA (Sharma et al. 2011), or the methodology presented in Pasetto, Chiosi & Kawata (2012) or Lowing et al. (2015). GALAXIA is a flexible population synthesis code for generating a synthetic stellar catalogue from an *N*-body or an analytical galaxy model over wide sections of the sky, with a sampling scheme which generates a smoothly distributed sample of stars. Synthetic catalogues generated from dynamical Galaxy models are essential for preparing to exploit the real *Gaia* catalogue and can be used to determine whether certain features within the Milky Way will be visible to *Gaia*.

In our previous work (Kawata et al. 2014b), we examined the kinematics of both the stellar and gas components around a transient, corotating spiral arm in a simulated barred spiral galaxy similar in size to the Milky Way. Although this arm is transient, similar arms recur during the evolution of the galaxy. We made predictions of observable kinematic signatures that may be visible in the Milky Way's Perseus arm if it is also a transient, recurrent and corotating spiral arm. We then compared our simulation with data from the Apache Point Galactic Evolution Experiment (APOGEE) and the maser sources from Reid et al. (2014) measured by the Bar and Spiral Structure Legacy survey and the Japanese VLBI (very long baseline interferometry) Exploration of Radio Astronomy, finding tentative agreement between our simulation and the observations. Owing to the low number of maser sources and the lack of distance information for the APOGEE stars, no firm conclusions could be drawn; however, it is encouraging to see similar features in both, including the possible signatures of a corotating spiral arm.

In this paper, we build upon the previous work by generating a stellar sample with different populations from the simulation data in Kawata et al. (2014b) and making mock observations of these stars taking into account the expected *Gaia* science performance estimates. The aim is not to make further predictions about the kinematics of transient, recurrent and corotating spiral arms but rather to examine whether these signatures remain visible in the *Gaia* data if they exist in the Milky Way.

2 SIMULATION

We use the simulated galaxy which is presented in Kawata et al. (2014b) and Grand, Kawata & Cropper (2015). The details of the numerical simulation code and the galaxy model are described in Kawata et al. (2014b). We briefly describe the galaxy model in this section. The galaxy is set up in isolated conditions, and consists of a gas and stellar disc but no bulge component. The discs are embedded in a static dark matter halo potential (Rahimi & Kawata 2012; Kawata et al. 2014b). The dark matter halo mass is $M_{\rm dm} = 2.5 \times 10^{12}\,{\rm M}_\odot$, and the dark matter density follows the density profile from Navarro, Frenk & White (1997), with a concentration parameter of $c = 10$. The stellar disc is assumed to follow an exponential surface density profile with the initial mass of $M_{\rm d,*} = 4.0 \times 10^{10}\,{\rm M}_\odot$, a radial scalelength of $R_{\rm d,*} = 2.5\,{\rm kpc}$ and a scale-height of $z_{\rm d,*} = 350\,{\rm pc}$. The gas disc is set up following the method of Springel, Di Matteo & Hernquist (2005), and has an exponential surface density profile with the scale-length of

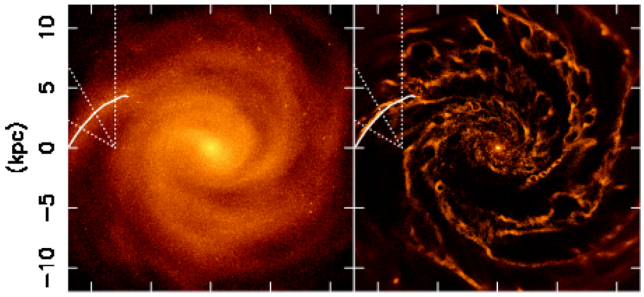

Figure 1. Snapshot of the simulated galaxy from Kawata et al. (2014b) which is also used in this paper. The left- (right-)hand panel shows the face-on view of the star (gas) particle distribution. The solid line indicates the position of the spiral arm identified. The observer is assumed to be located at $(x, y) = (-8, 0)$ kpc. Three line-of-sight directions ($l_{\rm LOS} = 90$, 120 and 150 deg) are highlighted with the dotted lines. The galaxy is rotating clockwise.

$R_{\rm d,g} = 8.0$ kpc. The total mass of the gas is 10^{10} M$_\odot$. The simulation comprises 10^6 gas particles and 4×10^6 star particles; therefore, each particle has a mass of 10^4 M$_\odot$. The resolution is sufficient to minimize numerical heating from Poisson noise (Fujii et al. 2011; Sellwood 2013). We employ a minimum softening length of 158 pc (equivalent to a Plummer softening length of 53 pc) with the spline softening and variable softening length for gas particles as suggested by Price & Monaghan (2007).

The radial profile of the mean metallicity of stars and gas is initially set by [Fe/H]$(R) = 0.2$–$0.05(R/1{\rm kpc})$, and the metallicity distribution function at each radius is centred on the mean metallicity value with the dispersion set to a Gaussian distribution of 0.05 dex for the gas and 0.2 dex for the stars. The stellar ages are set randomly between 0 and 10 Gyr for stars present at the beginning of the simulation.

The simulation was run for 1 Gyr from the initial conditions with the *N*-body smoothed particle hydrodynamics (SPH) code, GCD+ (e.g. Kawata & Gibson 2003; Rahimi & Kawata 2012; Barnes, Kawata & Wu 2012; Kawata et al. 2013, 2014a) without the inclusion of any continuous external inflow of gas for simplicity. In this paper, we use the same snapshot of the galaxy as used in Kawata et al. (2014b) which is taken at $t = 0.925$ Gyr, as this snapshot shows a spiral arm at a similar location to the Perseus arm of the Milky Way in the Galactic longitude range of $l = 90$–150 deg (see Fig. 1). We assume that the position and velocity of the Sun is known. We locate the observer at (−8,0,0) kpc as shown in Fig. 1, and the motion of the Sun is assumed to be the same as the circular velocity at 228 km s^{-1}.

The velocity dispersion for the *N*-body particles in the simulated galaxy at the Galactic radius, $7.5 \leq R_{\rm G} \leq 8.5$, is comparable to that for the stars in the Solar neighbourhood. We calculate the radial (σ_U), azimuthal (σ_V) and vertical (σ_W) velocity dispersion for the young and old particles at the Solar radius of the simulation, which is defined with the Galactic radius, $7.5 \leq R_{\rm G} \leq 8.5$ and $|z| \leq 0.5$ kpc. We define the young stars as the star particles with an age less than 0.5 Gyr, which are the star particles formed after the bar formation. As stated above, the simulation is only run for 0.925 Gyr and the particles older than 0.925 Gyr were created in the initial conditions. Thus, the old stars are defined as the particles with ages between 1 and 10 Gyr, which were created in the initial conditions with their age set randomly between 0 and 10 Gyr, and have since been kinematically heated by the formation of the bar. The analysed velocity dispersions are listed in Table 1. We compare the velocity dispersion from the simulation with the observed velocity dispersion in Holmberg, Nordström & Andersen (2009), which shows the velocity dispersion for stars older than 1 Gyr. The velocity dispersion in Holmberg et al. (2009) increases continuously with age. We list the velocity dispersion of the second youngest bin in fig. 7 of Holmberg et al. (2009), which approximately corresponds to the age of 1.5 Gyr, and the range of the velocity dispersion for the stars with an age of 2–10 Gyr, to compare respectively with the velocity dispersion of the young and old stars in the simulated galaxy. Although the radial and azimuthal velocity dispersion of the young star particles in the simulation are higher, the velocity dispersion of the old star particles in the simulation is well within the range given in Holmberg et al. (2009) for the observed velocity dispersions for the Solar neighbourhood stars.

Table 1. Radial (σ_U), azimuthal (σ_V) and vertical (σ_W) velocity dispersion of the simulation and observed values for the Milky Way (Holmberg et al. 2009).

	Simulation		Holmberg et al. (2009)	
Age	≤0.5 Gyr	1–10 Gyr	∼1.5 Gyr	2–10 Gyr
σ_U	30	39	∼26	∼23–50
σ_V	21	29	∼15	∼15–30
σ_W	8	20	∼10	∼10–30

However, we note that the aim of this study is to test if the *Gaia* data can identify the peculiar motion around the corotating spiral arm found in Kawata et al. (2014b). As in Kawata et al. (2014b), the simulation is not intended to reproduce the whole structure of the Milky Way. The pitch angle of the spiral arm in the simulation is 39 deg, which is much larger than the estimated pitch angle for the Perseus arm, e.g. 9.4 ± 1.4 deg (Reid et al. 2014).

It is worth discussing the strength of the simulated spiral arm, compared to the strength of the Perseus arm. Fig. 2 in Kawata et al. (2014b) shows the simulated arm has an amplitude of ∼0.12 in the $m = 2$ Fourier mode (normalized to the $m = 0$ mode). A pitch angle of 39 deg and amplitude of 0.12 is within the scatter of the pitch

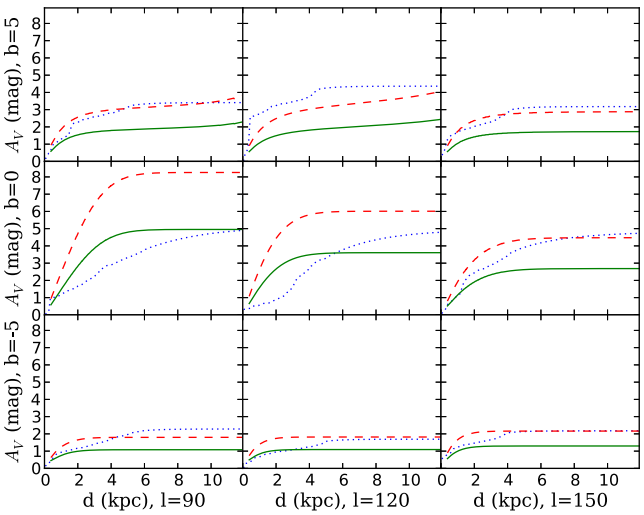

Figure 2. Extinction, A_V, for the 3D schlegel map without the reduction in the extinction by equation (1) (red dashed), the 3D Schlegel map with the reduction (green solid) and the 3D extinction map from Sale et al. (2014, blue dotted) for the lines of sight of the Galactic longitudes of $l = 90$ deg (left column), $l = 120$ deg (middle column), $l = 150$ deg (right column) and latitudes of $b = 5$ deg (top row), $b = 0$ deg (middle row), and $b = -5$ deg (bottom row).

angle/amplitude relation explored in fig. 8 in Grosbøl, Patsis & Pompei (2004). The local density enhancement of the Milky Way's Perseus arm is not currently well constrained. However, Benjamin et al. (2005) estimated the stellar density enhancement of the Centaurus arm is about 20 per cent using data from the *Spitzer* Galactic Legacy Mid-Plane Survey Extraordinaire.

As discussed in Kawata et al. (2014b), we measured the strength of the bar using a gravitational field method (e.g. Buta et al. 2005) described in Grand et al. (2012b), and obtained the bar strength $Q_{\rm b} = 0.15$, which is consistent with the lower end of the estimates of the Milky Way's bar strength, which is between $Q_{\rm b} = 0.17$ and 0.83 in table 1 of Romero-Gómez et al. (2011).

3 *GAIA* MOCK CATALOGUE

In Kawata et al. (2014b), the kinematics of the spiral arm shown in Fig. 1 are examined at three lines of sight $l_{\rm LOS} = 90$, 120 and 150 deg, with $b_{\rm LOS} = 0$ because of the lower extinction relative to other lines of sight. We do not include $l_{\rm LOS} = 180$ deg, because the distance to the spiral arm in our simulation is much further than the Perseus arm owing to the large pitch angle of the simulated galaxy. Predictions are made of the observational signatures of corotating spiral arms notably the difference in kinematic structure between the trailing near side and leading far side of the spiral arm. In general, in Kawata et al. (2014b, as also shown in Grand et al. 2014), the stars in the trailing near side rotate slower because they tend to be at the apocentre and migrate outwards, and the stars in the leading far side rotate faster as they tend to be at the pericentre and migrate inwards. There are however some stars which follow the opposite trend, leading to multiple populations seen in the rotational velocity in the leading far side; one faster, and one slower than the single population in the trailing near side. These features which will be discussed later may be caused by the corotation resonance of the spiral arm, and are visible at different galactic longitudes because the arm in the simulation corotates at all the examined radial range. However, in Kawata et al. (2014b), the spiral arm kinematics are examined using the full, error and extinction free *N*-body data and thus such trends, when present, are easy to identify.

In this section, we describe how we generate a sample of stars from the *N*-body model of Kawata et al. (2014b) to produce a mock *Gaia* catalogue. It is worth noting that the population synthesis code, GALAXIA (Sharma et al. 2011) provides a tool to generate stellar populations from *N*-body simulation data. However, because we plan to combine such a tool with our made-to-measure Galaxy modelling code, PRIMAL, we have developed our own simplified version of GALAXIA, a population synthesis code called SNAPDRAGONS (Stellar Numbers And Parameters Determined Routinely And Generated Observing *N*-body Systems). SNAPDRAGONSuses the same isochrones and extinction map as GALAXIA, but uses a different and simpler process to generate the stellar catalogue which is described in Section 3.2. SNAPDRAGONS allows us to add the expected *Gaia* errors more easily, and enables us to track the link between sampled stars and their parent *N*-body particle for our future studies, e.g. PRIMAL modelling of the Galactic disc by fitting tracers from multiple stellar populations, and identifying radially migrating stars and non-migrating stars trapped by the spiral arm (Grand et al. 2014).

3.1 Extinction

We use the extinction map of the Milky Way taken from GALAXIA (Sharma et al. 2011), which is a 3D polar logarithmic grid of the dust extinction constructed using the method presented in Bland-Hawthorn, Krumholz & Freeman (2010) and the dust maps from Schlegel et al. (1998), which we call the 3D Schlegel map. The same extinction is applied in Hunt & Kawata (2014) and more detail is given there. In an update from Hunt & Kawata (2014), we follow the reduction to the Schlegel E_{B-V} suggested in Sharma et al. (2014) such that

$$E_{B-V} = E_{B-V}\left(0.6 + 0.2\left(1 - \tanh\left(\frac{E_{B-V} - 0.15}{0.1}\right)\right)\right). \quad (1)$$

This reduction is made because it has been suggested (e.g. Arce & Goodman 1999; Yasuda, Fukugita & Schneider 2007) that the reddening is overestimated by the maps from Schlegel et al. (1998) by ∼1.3–1.5 in regions with high extinction with $A_V > 0.5$ ($E_{B-V} > 0.15$). This reduces extinction by ∼40 per cent for low-latitude high-extinction regions but has minimal effect on high-latitude low-extinction regions. In Fig. 2, we compared the 3D Schlegel map with and without this reduction term with the 3D extinction map from Sale et al. (2014) which is based upon photometry from the INT Photometric Hα Survey of the Northern Galactic Plane. Fig. 2 shows the comparison of extinction, A_V, for the 3D Schlegel map without the reduction of equations (1) (red dashed), the 3D Schlegel map with the reduction (green solid) and the 3D extinction map from Sale et al. (2014, blue dotted) for the lines of sight of the Galactic longitudes of $l = 90$ deg (left column), $l = 120$ deg (middle column), $l = 150$ deg (right column) and latitudes of $b = 5$ deg (top row), $b = 0$ deg (middle row) and $b = -5$ deg (bottom row). The values of A_0 from Sale et al. (2014) were used to calculate A_V at the nearest voxel to each line of sight using the approximation from Bailer-Jones (2011):

$$\begin{aligned} A_V \simeq A_0 &- 5.376 + 2.884(\log(T_{\rm eff})) - 0.4217A_0 \\ &- 0.3865(\log(T_{\rm eff}))^2 - 0.003\,74A_0^2 \\ &+ 0.1072(\log(T_{\rm eff}))A_0, \end{aligned} \quad (2)$$

assuming $\log(T_{\rm eff}) = 4750$ K, an average temperature for Red Clump stars (e.g. Puzeras et al. 2010; Bovy et al. 2014).

Fig. 2 demonstrates the uncertainties of the extinction at low Galactic latitudes, and the reduction term of equation (1) underestimates the extinction in some lines of sight compared with Sale et al. (2014). Therefore, we will present results with and without the reduction in the extinction by equation (1).

3.2 Population synthesis: SNAPDRAGONS

The goal of this population synthesis code is to split each *N*-body particle from the galaxy simulation into an appropriate number of stellar particles creating a mock catalogue of observable stars from our *N*-body model. We must choose an IMF and a set of isochrones with which to work. We choose a Salpeter IMF (Salpeter 1955) where the IMF, $\Phi(m)$, is defined in each mass interval dm as

$$\Phi(m)\,{\rm d}m = Am^{-(x+1)}{\rm d}m, \quad (3)$$

where $x = 1.35$ is the Salpeter index, and A is a constant for normalization in the desired mass range. We set this constant as

$$A_i = m_i\left(\int_{m_{*,\rm min}}^{m_{*,i,\rm max}} m^{-x}{\rm d}m\right)^{-1}, \quad (4)$$

where m_i is the *N*-body particle mass, $m_{*,i,\rm max}$ is the maximum initial mass of any surviving star and $m_{*,\rm min}$ is the minimum stellar mass to be considered. We make use of the Padova isochrones (e.g. Bertelli et al. 1994; Marigo et al. 2008), although the choice of isochrones

(and IMF) may be substituted with others with no change to the methodology.

It is worth noting that the Padova isochrones are available only for stellar masses above 0.15 $M_\odot$. GALAXIA for example uses the isochrones from Chabrier et al. (2000) to extend the mass limit down to 0.07 $M_\odot$, which is the hydrogen mass-burning limit. We set our lower limit on stellar mass as $m_{*,\min} = 0.1\ M_\odot$ to correspond with the simulation from Kawata et al. (2014b) and extrapolate from the Padova isochrones for $0.1 \leq M_\odot \leq 0.15$. It is relatively safe to do this because all such stars lie on the main sequence. Additionally, these exceedingly faint stars will not be visible at the distance of the spiral arms which are the focus of this work.

As discussed in Section 2, each *N*-body star particle in the simulated galaxy has been assigned an age and metallicity within the chemodynamical code GCD+, then it is made to evolve. When we examine the snapshot, each particle is matched to its nearest isochrone in both metallicity and age from the grid of isochrones which are extracted from GALAXIA. Once an isochrone is selected, we identify $m_{*,i,\max}$ from the isochrone. We then determine how many stars to sample from the *N*-body particle by integrating the IMF over the desired mass range;

$$N_\mathrm{s} = A \int_{m_{\star,i,<V_\mathrm{lim}}}^{m_{\star,i,\max}} m^{-(x+1)} \mathrm{d}m, \tag{5}$$

where $m_{\star,i,<V_\mathrm{lim}}$ is minimum mass required for the star particle to be brighter than our apparent magnitude selection limit, V_lim, taking into account the extinction value at the position of the parent particle. Stars smaller than $m_{\star,i,<V_\mathrm{lim}}$ are not used in the subsequent analysis, to save on computational time.

We then randomly sample stellar masses from the section of the isochrone N_s times. We have weighted the random selection by the IMF using the equation

$$m_\star = (R m_{\star,i,\max}^{-x} + (1-R) m_{\star,i,<V_\mathrm{lim}}^{-x})^{\frac{1}{-x}}, \tag{6}$$

where R is a random number between 0 and 1. The isochrones are comprised of discrete stellar data, and therefore we then interpolate within the nearest isochrone values of M_V and $V - I_c$ to determine $M_{V,*}$ and $V - I_{c*}$ for the generated m_*.

The number of stars sampled from each particle has to be an integer value. However, N_s calculated in equation (5) is not an integer value. Therefore, we compare the decimal component of N_s with another random number between 0 and 1, and if the random number is smaller than the decimal component of N_s we round up, otherwise we round down.

We calculate the exact stellar mass that is expected to be generated from a group of *N*-body star particles using the assumed IMF as

$$M_\mathrm{exp} = \sum_i A_i \int_{m_{\star,i,<V_\mathrm{lim}}}^{m_{\star,i,\max}} m_i^{-x} \mathrm{d}m, \tag{7}$$

where i represents an *N*-body star particle in the selected group. We also calculate the total mass of the stars which are generated from these particles;

$$M_\mathrm{gen} = \sum_i \sum_j^{N_s} m_{\star,j}. \tag{8}$$

Fig. 3 compares the generated stellar mass, M_gen, and the exact stellar mass, M_exp, within a square region of ± 5 deg around $(l, b) = (90, 0)$ at different distance bins. Fig. 3 shows the mean and one standard deviation of $M_\mathrm{gen}/M_\mathrm{exp}$ calculated using 100 different sequences of independently generated random numbers. Blue circles show the results of the methodology described above, which shows an excellent agreement between M_gen and M_exp. For comparison, if we only round N_s down (red crosses), M_gen becomes systematically lower than M_exp at larger distances where only a few bright stars are sampled from each particle. Therefore, it is important to statistically sample the decimal component of N_s.

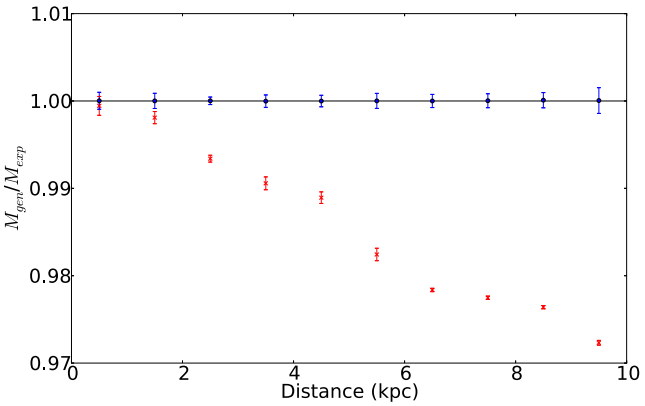

Figure 3. Mean difference between expected mass, M_exp, and generated mass, M_gen, with one standard deviation calculated using 100 different sequences of independently generated random numbers. Blue circles show the results for the methodology presented in Section 3.2. Red crosses show, for comparison, the results when considering only the integer component of N_s in equation (5).

The generated stars have the same position and velocity as their parent *N*-body particles. This method suffers from the discrete distribution of stars. However, if the selected volume is sufficiently sampled by enough *N*-body particles to resolve the structures of interest, the discreteness is not an issue. The region of the spiral arm focused on in this paper and the peculiar velocity structures within are well sampled by the *N*-body particles. Therefore, we do not think that this method of sampling affects the results in this work. However, in the case of phase-space structures which are poorly sampled by *N*-body particles e.g. in low-density regions or even in high-density regions, if the volume sampled is too small, the discreteness of the distribution becomes an issue. A more sophisticated method to smoothly distribute the generated stars in the phase space is applied in Lowing et al. (2015) based on the entropy-based binary decomposition (ENBID) code in Sharma & Steinmetz (2006). This is a powerful method to describe the phase-space distribution of stars from simulations that do not well resolve the targeted phase-space structure. This method could be included in the future version of SNAPDRAGONS.

3.3 Observational errors

Having generated the visible stellar catalogue, we then add observational errors based upon the *Gaia* Science Performance estimates.[1] We use the post-launch error estimates approximated from the estimates in pre-launch performance by Mercè Romero-Gómez (e.g. Romero-Gómez et al. 2015), provided through the *Gaia* Challenge collaboration.[2] For this work, while generating the stellar catalogue we produced stars only brighter than $V_\mathrm{lim} \leq 16$ mag, which is well within *Gaia*'s $G \leq 20$ mag magnitude limit for the astrometry. However, because we are interested in the Galactic radial and rotation

[1] http://www.cosmos.esa.int/web/Gaia/science-performance
[2] http://astrowiki.ph.surrey.ac.uk/dokuwiki/doku.php

velocity for the stars, which requires the full 6D phase-space information, we chose the lower magnitude limit where *Gaia*'s radial velocity spectrometer (RVS) can produce the reasonably accurate line-of-sight velocity. Note that the errors are added to the parallax, proper motion and line-of-sight velocities.

A full description of the method to add the pre-launch *Gaia* error is available in Hunt & Kawata (2014). However the *Gaia* science performance estimates have been revised after launch, and as such a correction must be made. The error in parallax has increased, and although it has little effect for stars with $v \leq 16$ mag with which we work in this paper, the coefficients within the equation to describe the pre-launch parallax performance (provided by Kazi, Antoja & DeBruijne (in 2014 October) by fitting to the new estimations on the *Gaia* science performance web page) are revised to

$$\sigma_\pi = (-11.5 + 706.1z + 32.6z^2)^{1/2} \times (0.986 + (1 - 0.986)(V - I_c)), \quad (9)$$

where

$$z = \max(10^{0.4(12-15)}, 10^{0.4(G-15)}), \quad (10)$$

correcting also the typo for equations (9) and (10) in Hunt & Kawata (2014).

Additionally, because of the loss of spectroscopic accuracy by $\sim$1.5 mag in the RVS post-launch performance, we also apply a correction to the error function for the end of mission radial velocity. We change the table[3] of values a and b, again determined by fitting the revised performance estimates on the *Gaia* science performance web page, for the equation

$$\sigma_{v_r} = 1 + b\, e^{a(V-14)}, \quad (11)$$

where a and b are constants dependant on the spectral type of the star. The new table along with the code to add the *Gaia* error is available online.[4]

4 RESULTS

As discussed in Section 3, it was shown in Kawata et al. (2014b) that in general the stars in the trailing near side of the spiral arm rotate slower than average because they tend to be at the apocentre, and the stars in the leading far side of the spiral arm rotate faster than average as they tend to be at the pericentre. However, there are groups of stars which follow different trends leading to multiple populations which will be discussed later. It is important to determine whether such features will still be visible in the *Gaia* catalogue, not just the error and extinction-free *N*-body model. In this section, we show the result of sampling these *N*-body data into stellar data, first looking at the properties of the resulting mock stellar catalogue, and then examining the spiral arm kinematics with the stellar data taking into account dust extinction and *Gaia* science performance estimates.

4.1 Population synthesis

In this section, we describe the stellar catalogue produced by SNAPDRAGONS, and show the resulting intrinsic colour–magnitude diagram (CMD) varying the area of the sky coverage. Fig. 4 shows the CMD for stars generated by SNAPDRAGONS from particles within a square region of ± 2 deg (upper) and ± 5 deg (lower) around $(l, b) = (90, 0)$ deg. The upper panel of Fig. 4 shows clearly the individual stellar isochrones because there are only a small number of *N*-body particles in the selected region, and each particle has only one age and metallicity. These problems are resolved when smoothing is applied in the phase-space distribution and age–metallicity distribution (e.g. Sharma et al. 2011). However, as discussed in Section 3.2 we deliberately avoid this smoothing to maintain the clear particle–star relation. The lower panel of Fig. 4 shows no such discrete structure, as there are sufficiently many particles to cover a broad range of stellar ages and metallicities in the CMD. Therefore, care is required with the resolution of the *N*-body simulation and the selection function if we discuss in detail the stellar population distribution in the CMD. However, this is unlikely to affect the study in this paper.

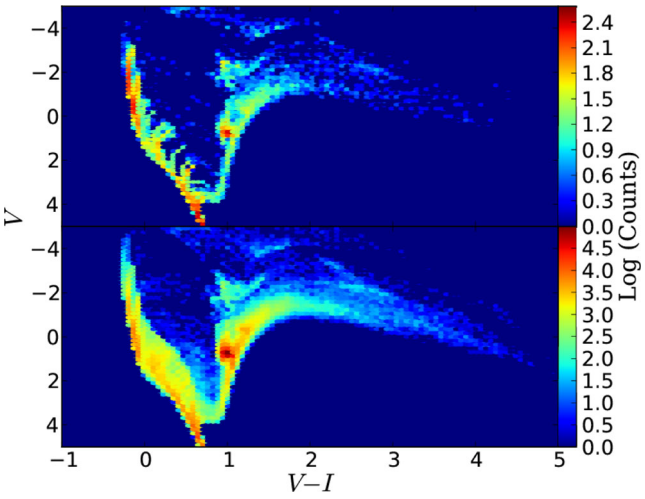

Figure 4. Intrinsic CMD for stars generated by SNAPDRAGONS from particles within a square region of ± 2 deg (upper) and ± 5 deg (lower) around $(l, b) = (90, 0)$ deg. Stars with apparent magnitude of $V \leq 16$ only are included.

We compared the star counts within a circular region of radius 5 deg around $(l, b) = (90, 0)$ for SNAPDRAGONS applied to our *N*-body simulation and GALAXIA using a version of the Besançon model. SNAPDRAGONS generated 205 621 stars with $V \leq 16$, and GALAXIA generated 251 880 stars with $V \leq 16$. The difference is caused by the structure in the underlying galaxy model. SNAPDRAGONS generates far fewer stars near to the observer owing to the low density interarm region close to the observer in the lines of sight. The Besançon model assumes axisymmetric stellar distribution, i.e. no azimuthal density contrasts (such as spiral arms and interarm regions) are applied. Therefore GALAXIA+Besançon generates substantially more stars at low distances.

4.2 Observable spiral arm kinematics

In this section, we examine if the possible kinematic signatures of corotating transient and recurrent spiral arms identified in Kawata et al. (2014b) will be visible in the *Gaia* data even given the dust extinction in the disc and *Gaia*'*s* science performance accuracy. A detailed analysis of the kinematics themselves was the focus of Kawata et al. (2014b), while this work is concerned with the visibility of this kinematic structure in the *Gaia* data. We examine the rotational velocities of the stars in the catalogue for different distances because in Kawata et al. (2014b) we found the rotation velocity is most affected by the transient corotating spiral arm. Then, we calculated the probability density function (PDF) of the

[3] http://www.cosmos.esa.int/web/Gaia/table-5
[4] https://github.com/mromerog/Gaia-errors

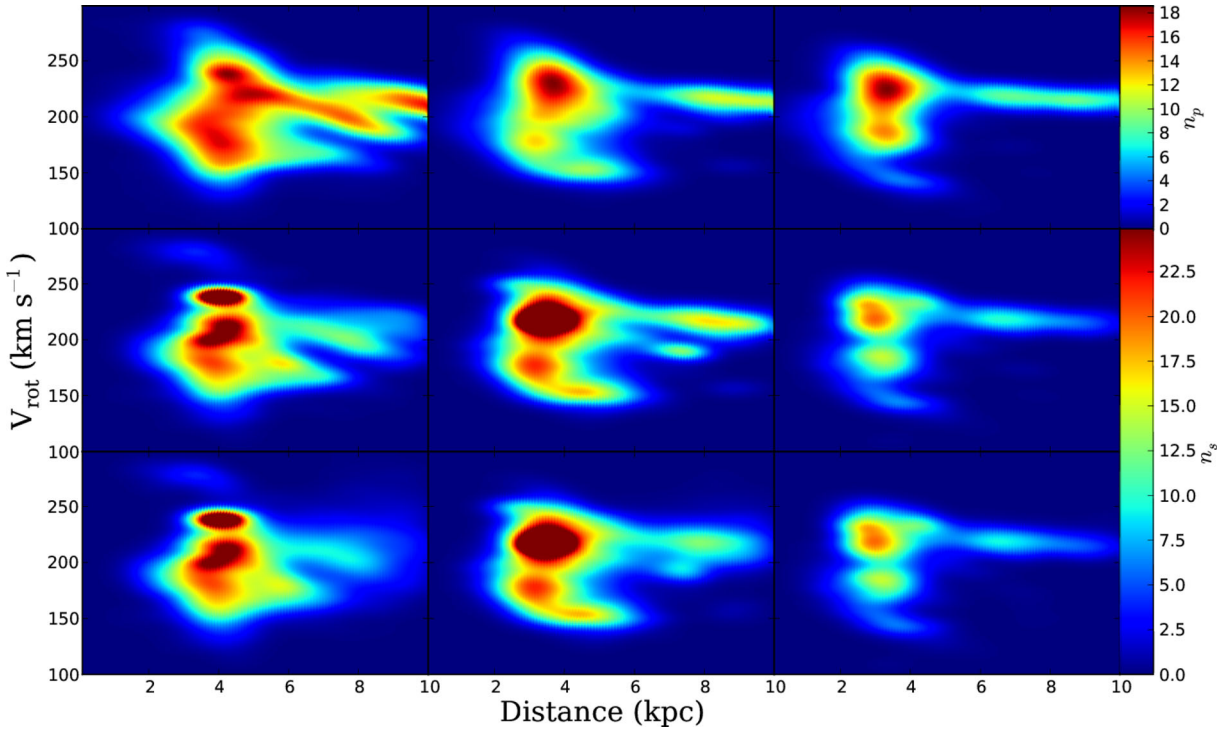

Figure 5. Smoothed linear scale contour plot of heliocentric distance against galactocentric rotation velocity of simulation particles (upper), selected SNAPDRAGONS stars (middle) and selected SNAPDRAGONS stars observed with *Gaia* error (lower) within a square region of ±5 deg around $(l, b) = (90, 0)$ (left), $(l, b) = (120, 0)$ (middle) and $(l, b) = (150, 0)$ (right). For the SNAPDRAGONS stars (middle and lower panels), a limited selection of $M_V \leq -1$ calculated using V and $d_{\rm obs}$ and assuming a known extinction, along with $\sigma_{v_{\rm r}}/(v_{\rm r} \times d_{\rm obs}) \leq 0.15$ is shown to avoid overly dense populations of fainter stars at smaller distances. This is to visualize the data set, and these faint stars contribute to the subsequent analysis. The colour scale shows number density of N-body particles (upper) and SNAPDRAGONS stars (middle and lower) in arbitrary units.

rotation velocity of stars behind and in front of the spiral arm using Kernel density estimation (KDE) which we are using as a desirable alternative to histograms (e.g. Wasserman 2006).

Fig. 5 shows a smoothed contour plot of the galactocentric rotational velocity against observed heliocentric distance for particles and stars within a square region of ±5 deg around $(l, b) = (90, 0)$ (left), $(l, b) = (120, 0)$ (middle) and $(l, b) = (150, 0)$ (right). This compares the kinematics of the underlying N-body model (upper) with the stellar catalogue generated with SNAPDRAGONS, before (middle) and after (lower) the addition of the errors from the *Gaia* science performance estimates. Owing to the high percentage of low-mass and luminosity stellar types which would dominate the selected region and saturate the plot at small distances, we have made cuts to our sample to visualize the underlying kinematic structure from the stellar catalogue. We have first cut the sample of stars in all three lines of sight with absolute magnitude, $M_V \leq -1$, calculated from the apparent magnitude V and observed distance $d_{\rm obs}$, assuming the dust extinction is known. We then cut with $\sigma_{v_{\rm los}}/(v_{\rm los} \times d_{\rm obs}) \leq 0.015\,{\rm kpc}^{-1}$ to select the stars with lower error in the line-of-sight velocities at a smaller distance to generate similar quantities of data at different distance scales. This selection function selects bright stars which are a mix of young blue stars and old red stars. The number of stars selected are 11 903 for $(l, b) = (90, 0)$, 12 989 for $(l, b) = (120, 0)$ and 5794 for $(l, b) = (150, 0)$. This is purely for illustration purposes and we are not suggesting that this is a desirable selection function with which to analyse the kinematics. The upper panels of Fig. 5 show the different kinematic structure in the N-body model at the different lines of sight. These are the same data as those shown in the top panels of fig. 4 from Kawata et al. (2014b). Note that the density colour scale for the N-body data is different from the stellar data in the middle and lower panels.

The middle row of panels of Fig. 5 show the velocities of the selected stars, which appear slightly different from those of the N-body data owing to the selection function. While the generated stars have the same position and velocities as their parent N-body particles, the dust extinction, the magnitude cut of $V \leq 16$ mag and the above-mentioned selection of bright stars with the velocity error limit are applied. Therefore, the middle panels are different from the top panels. Especially, owing to the strong extinction in the plane, not all the N-body data in the top panel are 'visible' in the selected stars in the middle panel. While the general shape of the distribution has been recovered, at $(l, b) = (90, 0)$ deg (middle left), the fast rotating stars within the arm dominate the density scale and wash out the rest of the plot slightly. At $(l, b) = (120, 0)$ deg (middle), although there is some saturation around 220 km s^{-1} the kinematic structure is clearly visible and is a good match to the particle data. Similarly at $(l, b) = (150, 0)$ deg (middle right), despite the lower number of counts, the kinematic structure is clearly shown.

The lower panels of Fig. 5 show the error affected rotation velocity and distance for the selected stars taking *Gaia* science performance estimates into account. The rotation velocity is calculated from the observed parallax, proper motion and line-of-sight velocities. At $(l, b) = (90, 0)$ (lower left), the shape of the distribution remains relatively unchanged, with the main loss in accuracy occurring around $d_{\rm obs} \approx 7-10$ kpc. The recovery of the kinematic structure around the spiral arm around $d_{\rm obs} \approx 4$ kpc remains almost identical to the case without observational errors. At

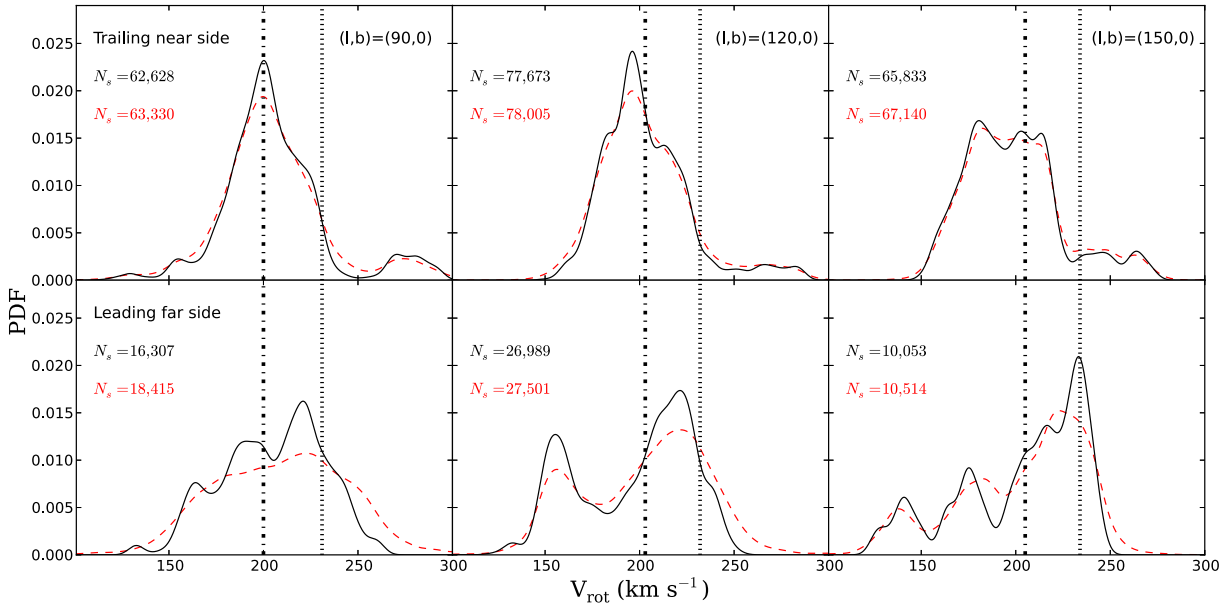

Figure 6. Comparison of the distribution of galactocentric rotational velocities for the stars generated by SNAPDRAGONS within a square region of ±5 deg around $(l, b) = (90, 0)$ (left), $(l, b) = (120, 0)$ (middle) and $(l, b) = (150, 0)$ (right) in the trailing near side (upper) and leading far side (lower) of the spiral arm which meet the $V \leq 16$ selection limit when applying the reduction in the extinction with equation (1). The black solid curve shows the true velocities, and the red dashed curve shows the distribution once the *Gaia* errors have been applied. The number of stars, N_s, used to construct the PDFs is given in each panel for the velocities without (black) and with (red) the inclusion of error. The vertical lines show the circular velocity (dotted) and the mean rotation velocity (dash-dotted) at the radius of the spiral arm.

$(l, b) = (120, 0)$ (lower middle), the visible loss of accuracy is again in the outer region of $d_{\rm obs} \approx 7-10$ kpc, with the region containing the spiral arm remaining very similar to that of the error-free case. At $(l, b) = (150, 0)$ (lower right), the entire distribution remains very similar to the middle right panel, the case without *Gaia* like observational errors.

Fig. 6 shows the PDFs, with a KDE bandwidth of 4, for the rotational velocity of the stars in the catalogue within a square region of ±5 deg around $(l, b) = (90, 0)$ (left), $(l, b) = (120, 0)$ (middle) and $(l, b) = (150, 0)$ (right) in the trailing near side, between 1 and 2 kpc closer than the centre of the arm (upper) and leading far side between 1 and 2 kpc further than the centre of the arm (lower) using the 3D Schlegel map with the extinction reduced with equation (1). These heliocentric observed distance bins were chosen as they show the discussed structure most clearly; the same features are present closer to the arm but are less clear. The number of stars, N_s, used to construct the PDFs is given in each panel of Fig. 6 for the velocities without (black) and with (red) the inclusion of error. The centre of the arm was determined to be at $d = 4.0$ kpc at $(l, b) = (90, 0)$, $d = 3.4$ kpc at $(l, b) = (120, 0)$ and $d = 3.3$ kpc at $(l, b) = (150, 0)$. Note that Fig. 6 uses all the stars with $V \leq 16$ mag, not applying the selection function used for illustration purposes in Fig. 5. At all three lines of sight, Fig. 6 shows a clear difference in the distribution of velocities for the 'true' data (black solid) when comparing the different observed distances, as shown in Kawata et al. (2014b). This is a positive outcome considering the loss of data from the dust extinction. When comparing the 'true' (black solid) stellar catalogue data with the stellar data taking into account dust extinction and *Gaia*'s expected errors (red dashed), a general smoothing out of the structure is evident in the 'observed' data. The upper panels of Fig. 6 showing the trailing near side of the arm show very similar PDFs when comparing the true and observed stellar data, whereas the lower panels showing the leading far side show an information loss, especially at $(l, b) = (90, 0)$, where the three peaks are no longer resolved. This is to be expected because of the higher distances and therefore additional extinction. However, at $(l, b) = (120, 0)$ and $(150, 0)$ even on the far side of the spiral arm the structure within the distribution is still clearly visible. Fig. 7 shows the same as Fig. 6, using the higher extinction values of the 3D Schlegel map without the reduction term of equation (1). The features in Fig. 7 remain very similar to Fig. 6 despite the difference in extinction. There is a significant reduction in the number of observed stars for the 3D Schlegel map without the reduction in extinction. It is therefore important to note that the assumed extinction model will have a large effect on the mock catalogue. However, it is encouraging for the interpretation of the *Gaia* data that the same peculiar kinematic features are visible with this higher extinction estimate. Owing to the similarity between Figs 6 and 7, the subsequent discussion will focus on Fig. 6.

When comparing the 'observed' data in Fig. 6 in front and behind the spiral arms, we see a clear difference in the PDF at all three lines of sight. In each case, the PDF in the trailing near side of the spiral arm forms a single central peak similar to the mean rotation velocity, with a small tail towards faster rotation velocities whereas the leading far side of the spiral arm shows a broader distribution of velocities with a peak velocity faster than the peak for the trailing near side. The difference is particularly apparent at $(l, b) = (120, 0)$ deg where the leading far side shows two clear peaks, one faster and one slower than the single peak in the trailing near side. This bimodal distribution can also be seen in the lower middle panel of Fig. 5 between 4.39 and 5.39 kpc (although note that Fig. 5 uses a different selection function). Also at $(l, b) = (150, 0)$ deg, the single broad peak in the trailing near side is easily distinguishable from the leading far side which shows three peaks. These three peaks are also partially visible in the lower right panel of Fig. 5 between 4.29 and 5.29 kpc. These features all match those observed in Kawata et al.

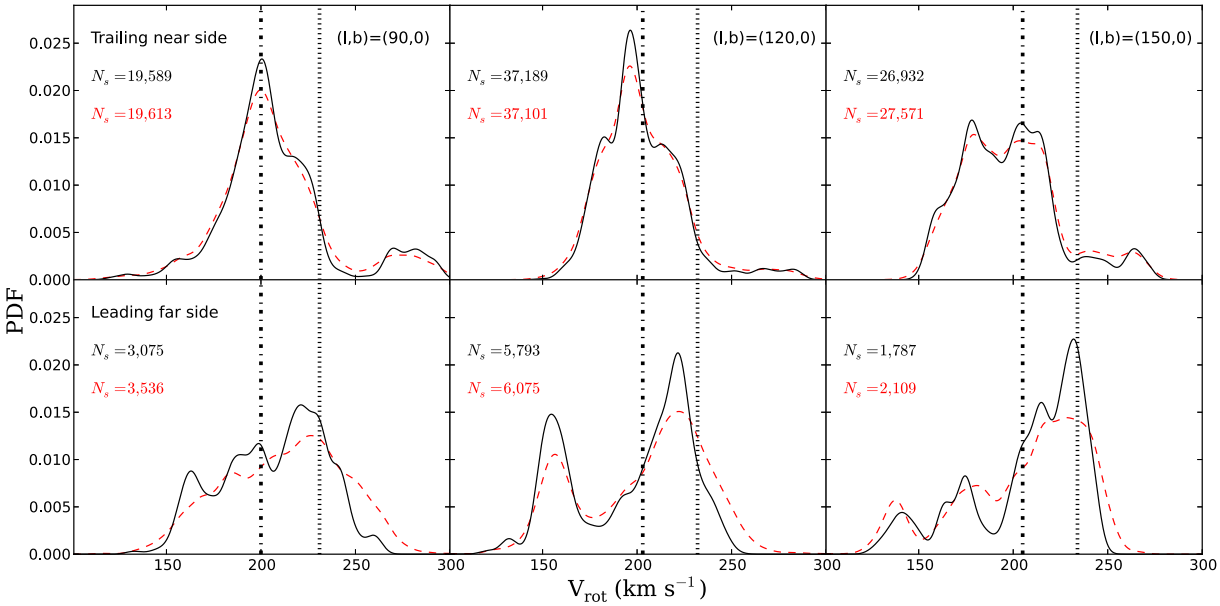

Figure 7. As for Fig. 6 except using the 3D Schlegel map without the reduction in the extinction given by equation (1).

(2014b) despite the addition of dust extinction and observational errors to the data.

In general, as shown in Grand et al. (2014), the stars in the leading side rotate faster as they tend to be at pericentre phase and migrating inwards, and stars in the trailing side rotate slower as they tend to be at apocentre phase and migrating outwards. This explains the single large peak in the trailing side, and the largest peak on the leading side which has a higher rotational velocity than the single peak on the trailing side as shown in Fig. 6. However, when the transient spiral arm starts forming, stars which are close to the arm on the trailing side and are close to the pericentre phase are accelerated towards the arm, passing through and then slowing down as they reach the apocentre on the leading side as discussed in Kawata et al. (2014b). These stars correspond to the 'slower' peaks visible in the lower panels of Fig. 6. Similarly, the stars which are close to the arm and close to the apocentre phase on the leading side are decelerated by the arm, and are overtaken by the arm. Then they are accelerated again by the arm once they are on the trailing side at pericentre phase, which corresponds to the small tail present at high velocities in the upper panels of Fig. 6. The difference in the rotation velocity distribution between the leading and trailing side of the spiral arm seen in Figs 5 and 6 is that the latter population is smaller than the former. It appears that it is easier for stars to escape from the arm on the leading side than the trailing side. From our analysis of *N*-body simulations, this appears to be a common feature of transient and corotating spiral arms.

Comparetta & Quillen (2012) propose that the radial overlap of multiple longer lived patterns moving at different pattern speeds can reproduce the transient spiral features, which when strong enough can lead to radial migration away from the corotation radius associated with corotating spiral arms as seen, for example in Grand et al. (2012a,b). In such a scenario, the spiral arm features are corotating, which may give rise to the coexistence of many inner and outer Lindblad resonances in a range of radii and lead to the features visible in Figs 5–7. However, further analysis of the spiral arms in *N*-body simulations is required before drawing firm conclusions on the mechanism that generates such kinematic signatures: we will address this in future studies.

From Figs 5–7, we find that *Gaia*'*s* scientific accuracy ought to be sufficient to examine the kinematic structure of the nearby spiral arms in the Milky Way, even on the far side of the arm. Figs 6 and 7 both show clear differences in the kinematics in the leading and trailing sides of the spiral arm, notably the difference in the number and locations of the peaks, and the small high-velocity tail present in the trailing near side. The comparison between the middle and lower panels of Fig. 5 shows little difference, implying that the observational error from *Gaia* will have limited effect on our ability to study the kinematics of the spiral arms. Further examination of galaxy models constructed using the different theories of spiral arm formation will be essential to determine the distinct kinematic signatures of each theory.

5 SUMMARY

We observed our *N*-body/SPH simulation of a Milky Way-like barred spiral galaxy to create a mock *Gaia* stellar catalogue, with particular interest in the stellar kinematics in and around the spiral arms. We focused on the same three lines of sight in the disc plane as Kawata et al. (2014b), $(l, b) = (90, 0)$, (120, 0) and (150, 0) deg and analysed the galactocentric rotational velocities of the selected stars as a function of the distance from the observer. In agreement with existing literature on *N*-body spiral galaxy simulations, the spiral arm features seen in the stellar mass in our model are transient, recurrent and corotating, i.e. the spiral arm is rotating at the circular velocity of the stars at the selected lines of sight.

We show that the structure in the kinematics identified in Kawata et al. (2014b) remains visible after the inclusion of dust extinction and observational errors based upon *Gaia* science performance estimates. Although the inclusion of these observational effects makes the trends less clear, they are still observable in the mock *Gaia* data in front of, inside and behind the spiral arm. The structure on the trailing near side is relatively unchanged, whereas the structure on the leading far side is, naturally, more affected, although the bimodal (or more) and broader distribution of the rotation velocities is still clearly visible. Because we believe that these kinematic signatures are indications of transient and corotating spiral arms owing to the

corotation resonance at all radii, we predict they should be visible in the *Gaia* data at different longitudes if the Milky Way's Perseus arm is also a transient and corotating spiral arm.

Encouraged by the success of this study, we intend to repeat the analysis with simulated galaxies which use different theories of spiral structure formation, for example test particle simulations (e.g. Minchev & Quillen 2008; Minchev et al. 2010; Minchev & Famaey 2010; Faure, Siebert & Famaey 2014; Antoja et al. 2014) and *N*-body simulations with a fixed spiral arm potential (e.g. Wada, Baba & Saitoh 2011). From these analyses, we expect to make predictions of the kinematic signatures of different spiral arm theories, which can be tested by the *Gaia* stellar catalogue.

ACKNOWLEDGEMENTS

We thank the anonymous referee for their thorough comments which helped to improve the method and the manuscript. We gratefully acknowledge the support of the UK's Science & Technology Facilities Council (STFC Grant ST/H00260X/1 and ST/J500914/1). The calculations for this paper were performed on Cray XT4 at Center for Computational Astrophysics, CfCA, of the National Astronomical Observatory of Japan and the DiRAC facilities (through the COSMOS consortium) including the COSMOS Shared Memory system at DAMTP, University of Cambridge operated on behalf of the STFC DiRAC HPC Facility. This equipment is funded by BIS National E-infrastructure capital grant ST/J005673/1 and STFC grants ST/H008586/1, ST/K00333X/1 & ST/J001341/1. The authors acknowledge the use of the IRIDIS High Performance Computing Facility, and associated support services at the University of Southampton. We would also like to thank PRACE for the use of the Cartesius facility. This work was carried out, in part, through the *Gaia* Research for European Astronomy Training (GREAT-ITN) network. The research leading to these results has received funding from the European Union Seventh Framework Programme ([FP7/2007-2013] under grant agreement number 264895). DK acknowledges the generous support and hospitality of the Kavli Institute for Theoretical Physics (KITP), University of California Santa Barbara during the 'Galactic Archaeology and Precision Stellar Astrophysics' programme, where some of this research was performed. This research was supported in part by the National Science Foundation under Grant No. NSF PHY11-25915. We would also like to thank Mercè Romero-Gómez and Francesca Figueras for providing the subroutine to calculate the *Gaia* performance errors, including the update to post-launch estimates, Sanjib Sharma for providing the GALAXIA extinction maps and isochrones and Sami Niemi for the suggestion of using KDE's to visualize the velocity distributions.

REFERENCES

Abedi H., Mateu C., Aguilar L. A., Figueras F., Romero-Gómez M., 2014, MNRAS, 442, 3627
Antoja T. et al., 2014, A&A, 563, A60
Arce H. G., Goodman A. A., 1999, ApJ, 512, L135
Baba J., Saitoh T. R., Wada K., 2013, ApJ, 763, 46
Bailer-Jones C. A. L., 2011, MNRAS, 411, 435
Bailer-Jones C. A. L. et al., 2013, A&A, 559, A74
Barnes D. J., Kawata D., Wu K., 2012, MNRAS, 420, 3195
Benjamin R. A. et al., 2005, ApJ, 630, L149
Bertelli G., Bressan A., Chiosi C., Fagotto F., Nasi E., 1994, A&AS, 106, 275
Bland-Hawthorn J., Krumholz M. R., Freeman K., 2010, ApJ, 713, 166
Bottema R., 2003, MNRAS, 344, 358
Bovy J. et al., 2014, ApJ, 790, 127
Buta R., Vasylyev S., Salo H., Laurikainen E., 2005, AJ, 130, 506
Carlberg R. G., Freedman W. L., 1985, ApJ, 298, 486
Chabrier G., Baraffe I., Allard F., Hauschildt P., 2000, ApJ, 542, 464
Comparetta J., Quillen A. C., 2012, preprint (arXiv:1207.5753)
D'Onghia E., Vogelsberger M., Hernquist L., 2013, ApJ, 766, 34
Dame T. M., Hartmann D., Thaddeus P., 2001, ApJ, 547, 792
de Bruijne J. H. J., 2012, Ap&SS, 341, 31
Dobbs C., Baba J., 2014, PASA, 31, 35
Drimmel R., Spergel D. N., 2001, ApJ, 556, 181
Drimmel R., Cabrera-Lavers A., López-Corredoira M., 2003, A&A, 409, 205
Faure C., Siebert A., Famaey B., 2014, MNRAS, 440, 2564
Fujii M. S., Baba J., Saitoh T. R., Makino J., Kokubo E., Wada K., 2011, ApJ, 730, 109
Grand R. J. J., Kawata D., Cropper M., 2012a, MNRAS, 421, 1529
Grand R. J. J., Kawata D., Cropper M., 2012b, MNRAS, 426, 167
Grand R. J. J., Kawata D., Cropper M., 2013, A&A, 553, A77
Grand R. J. J., Kawata D., Cropper M., 2014, MNRAS, 439, 623
Grand R. J. J., Kawata D., Cropper M., 2015, MNRAS, 447, 4018
Grosbøl P., Patsis P. A., Pompei E., 2004, A&A, 423, 849
Hanson R. J., Bailer-Jones C. A. L., 2014, MNRAS, 438, 2938
Holmberg J., Nordström B., Andersen J., 2009, A&A, 501, 941
Hunt J. A. S., Kawata D., 2013, MNRAS, 430, 1928
Hunt J. A. S., Kawata D., 2014, MNRAS, 443, 2112
Hunt J. A. S., Kawata D., Martel H., 2013, MNRAS, 432, 3062
Jordi C. et al., 2010, A&A, 523, A48
Kalberla P. M. W., Kerp J., 2009, ARA&A, 47, 27
Katz D. et al., 2011, EAS Publ. Ser., 45, 189
Kawata D., Gibson B. K., 2003, MNRAS, 340, 908
Kawata D., Okamoto T., Gibson B. K., Barnes D. J., Cen R., 2013, MNRAS, 428, 1968
Kawata D., Gibson B. K., Barnes D. J., Grand R. J. J., Rahimi A., 2014a, MNRAS, 438, 1208
Kawata D., Hunt J. A. S., Grand R. J. J., Pasetto S., Cropper M., 2014b, MNRAS, 443, 2757
Lin C. C., Shu F. H., 1964, ApJ, 140, 646
Lindegren L., Lammers U., Hobbs D., O'Mullane W., Bastian U., Hernández J., 2012, A&A, 538, A78
Lowing B., Wang W., Cooper A., Kennedy R., Helly J., Cole S., Frenk C., 2015, MNRAS, 446, 2274
Luri X. et al., 2014, A&A, 566, A119
Marigo P., Girardi L., Bressan A., Groenewegen M. A. T., Silva L., Granato G. L., 2008, A&A, 482, 883
Marshall D. J., Robin A. C., Reylé C., Schultheis M., Picaud S., 2006, A&A, 453, 635
Minchev I., Famaey B., 2010, ApJ, 722, 112
Minchev I., Quillen A. C., 2008, MNRAS, 386, 1579
Minchev I., Boily C., Siebert A., Bienayme O., 2010, MNRAS, 407, 2122
Minchev I., Famaey B., Quillen A. C., Di Matteo P., Combes F., Vlajić M., Erwin P., Bland-Hawthorn J., 2012, A&A, 548, A126
Nakanishi H., Sofue Y., 2003, PASJ, 55, 191
Navarro J. F., Frenk C. S., White S. D. M., 1997, ApJ, 490, 493
Pasetto S., Chiosi C., Kawata D., 2012, A&A, 545, A14
Price D. J., Monaghan J. J., 2007, MNRAS, 374, 1347
Puzeras E., Tautvaišienė G., Cohen J. G., Gray D. F., Adelman S. J., Ilyin I., Chrniy Y., 2010, MNRAS, 408, 1225
Quillen A. C., Dougherty J., Bagley M. B., Minchev I., Comparetta J., 2011, MNRAS, 417, 762
Rahimi A., Kawata D., 2012, MNRAS, 422, 2609
Reid M. J. et al., 2014, ApJ, 783, 130
Rix H.-W., Bovy J., 2013, A&AR, 21, 61
Robin A. C. et al., 2012, A&A, 543, A100
Roca-Fàbrega S., Valenzuela O., Figueras F., Romero-Gómez M., Velázquez H., Antoja T., Pichardo B., 2013, MNRAS, 432, 2878
Romero-Gómez M., Athanassoula E., Antoja T., Figueras F., 2011, MNRAS, 418, 1176

Romero-Gómez M., Figueras F., Antoja T., Abedi H., Aguilar L., 2015, MNRAS, 447, 218
Roškar R., Debattista V. P., Quinn T. R., Wadsley J., 2012, MNRAS, 426, 2089
Roškar R., Debattista V. P., Loebman S. R., 2013, MNRAS, 433, 976
Sale S. E., Magorrian J., 2014, MNRAS, 445, 256
Sale S. E. et al., 2014, MNRAS, 443, 2907
Salpeter E. E., 1955, ApJ, 121, 161
Schlegel D. J., Finkbeiner D. P., Davis M., 1998, ApJ, 500, 525
Sellwood J. A., 2011, MNRAS, 410, 1637
Sellwood J. A., 2013, ApJ, 769, L24
Sellwood J. A., Carlberg R. G., 1984, ApJ, 282, 61
Sellwood J. A., Carlberg R. G., 2014, ApJ, 785, 137
Shapley H., Curtis H. D., 1921, Bull. Natl. Res. Counc., 2, 171
Sharma S., Steinmetz M., 2006, MNRAS, 373, 1293
Sharma S., Bland-Hawthorn J., Johnston K. V., Binney J., 2011, ApJ, 730, 3
Sharma S. et al., 2014, ApJ, 793, 51
Springel V., Di Matteo T., Hernquist L., 2005, MNRAS, 361, 776
Toomre A., 1981, in Fall S. M., Lynden-Bell D., eds, Structure and Evolution of Normal Galaxies. Cambridge Univ. Press, Cambridge, p. 111
Wada K., Baba J., Saitoh T. R., 2011, ApJ, 735, 1
Wasserman L., 2006, Springer Texts in Statistics: All of Nonparametric Statistics. Springer-Verlag, New York
Wilczynski E. J., 1896, ApJ, 4, 97
Yasuda N., Fukugita M., Schneider D. P., 2007, AJ, 134, 698

This paper has been typeset from a TEX/LATEX file prepared by the author.